Ridgecrest Aftershocks at Coso Suppressed by Thermal Destressing

Kyungjae Im[1*], Jean-Philippe Avouac[1], Elías R. Heimisson[1], and Derek Elsworth[2]

[1]Geology and Planetary Science Division, California Institute of Technology, Pasadena, CA 91125, United States

[2] Energy and Mineral Engineering & Geosciences, EMS Energy Institute, and G3 Center, Pennsylvania State University, University Park, PA 16802, United States

*Correspondence to kjim@caltech.edu

Geothermal and volcanic areas are particularly prone to earthquake triggering[1,2]. The Coso geothermal field lies just north of the surface ruptures driven by the 2019 Ridgecrest M7.1 earthquake in an area where coseismic stress changes should have triggered aftershocks[3,4]. Surprisingly, a gap of aftershocks is observed there[4]. Here we show that 30 years of geothermal heat production at Coso depleted shear stresses within the geothermal reservoir. Thermal contraction of the reservoir initially induces significant seismicity, as observed in Coso geothermal reservoir, but it eventually contributed to depleting the stress available to drive the aftershocks during the Ridgecrest sequence. This destressing induced an active transition in its faulting style and impeded aftershock triggering. Such a destressed zone could, in principle, impede the propagation of a large earthquake.

The M_w 6.4 and 7.1 2019 Ridgecrest earthquakes triggered an intense sequence of aftershocks, which extended well North of the Coso volcanic area[5] (Fig. 1a). The seismicity coincides approximately with a northwest-trending lobe of Coulomb stress increase due to the M_w 7.1 mainshock[3] (Fig. 1b). The lack of aftershocks within the geothermal field area, which lies within this lobe of increased Coulomb stress is particularly striking[4] (Fig. 1). The gap of aftershocks at the Coso is unexpected as geothermal and volcanic areas are prone to remote triggering[6,] and geothermal operations can trigger intense seismicity[6-8]. Hereafter, we first demonstrate that this feature is real, and next, we use numerical simulations to show that it resulted from destressing due to the geothermal operation.

The lack of aftershocks at the Coso could be interpreted to reflect the locally shallower seismogenic depth range. Seismicity indeed cuts off at a particularly shallow depth of ~4km within the Coso field area (Fig. 1c), probably due to a shallow brittle-ductile transition due to the large temperature gradient[9]. Away from the Coso, the seismicity extends to the typical 10-15km depth of the seismogenic zone in California[10]. According to this explanation, we would expect a rate of aftershocks about 3-4 times lower at the Coso than elsewhere. However, even if we assume that the after-Ridgecrest seismicities are entirely aftershock (i.e., no contribution from the geothermal operation), the catalog shows an aftershocks rate ~20 times lower than in the areas immediately northwest or southeast of the geothermal field (Extended Data Fig. 1). We, therefore, conclude that the lack of aftershocks truly reflects a lower sensitivity of the geothermal field to static triggering. A recent study[11] based on a local seismic network reports more aftershocks at Coso than observed by the regional network. These data, once declustered, show that areas around the geothermal field actually experienced an increased rate of seismicity following the Ridgecrest earthquake. However, although the reservoir itself was included in the analysis, it could not be independently resolved due to the declustering. Another recent study with non-delcustered local seismic network data shows that the Ridgecrest earthquake did not impact the total seismicity rate within the reservoir[12].

Geothermal power production at the Coso started in 1987 with an electrical power capacity of 230 MW[13]. This large-scale operation induced significant ground deformation and seismicity. Subsidence measured using interferometric synthetic aperture radar (InSAR) exceeded 14 cm over the injection area between September 1993 and June 1998[14] and was most likely driven by both thermal contraction and pressure depletion as commonly observed over other geothermal fields[15]. There may also be natural tectonic or magmatic sources of vertical deformation in the Coso area[16], but it seems improbable that they are at play to explain the deformation signal measured from InSAR due to its strong correlation with the geothermal field operation. Recent InSAR observations show continued subsidence but at a lower rate (Fig. 2f).

The paucity of aftershocks during the 2019 earthquake sequence is surprising as the Coso reservoir has been seismically active since the beginning of geothermal field development in 1981[10] (grey circles, Fig. 1a&c). It is informative to consider the time evolution of seismicity within the Coso reservoir prior to 2019. The overall picture is that seismicity ramped up significantly when geothermal power production started in 1987 to peak after ~10 years of production (Fig. 1d). We can identify a spatio-temporal evolution of seismicity reflecting the details of the geothermal field development (Extended Data Fig. 2). An early transient peak in 1984 likely coincides, for example, with a stimulation or testing phase. A more recent peak is due to the development of the East Flank area after 2000. The overall evolution is dominated by the seismicity within the main field, which gradually increased and peaked after ~10 years from the beginning of geothermal production and decreased significantly afterward.

Reservoir pressure has been monotonically declining during production[17], a feature consistent with production exceeding injection (Fig. 2a). The pressure drop must have induced a gradual decrease of Coulomb stress (effective normal stress increase), so it is incapable of explaining the sustained seismicity observed in the reservoir. Hence, another effect that increases Coulomb stress, such as thermal destressing, is required. Thermo-poro-elastic stress changes can be significant due to elastic coupling[18] and can trigger seismicity at relatively large distances from the boreholes[18,19]. An initial flow test in the Coso area showed a gradual permeability increase associated with an injection pressure decline of ~0.5 MPa in 40 days[20]. This observation also points to the dominating thermal effect. Fracturing and faulting induced by thermal contraction indeed tend to enhance permeability[21]. By contrast, the pressure reduction should have prevented faulting and allowed for fracture closing, resulting in a permeability decrease.

Thermal effects evolve slowly and can considerably modify the state of stress[21-23] and could affect the depth of the brittle-ductile transition. The seismicity in the reservoir area clearly migrated to a greater depth during the field operation, as would be expected from reservoir cooling (Fig. 2c). There is also a hint, in the time evolution of focal mechanisms within the Coso area[24], that the stress field was indeed significantly altered during the geothermal production. The seismicity decline after the peak in the 1990s coincides with an increase in the diversity of focal mechanisms and the proportion of normal faulting events (Extended Data Fig. 3). Thus, we hypothesize that the cumulative stress changes induced by geothermal heat production from the Coso since 1987 impeded earthquake triggering during the Ridgecrest earthquake sequence of 2019.

We model the geomechanical effect of the geothermal operation using the thermo-hydro-mechanical simulator Tough-FLAC[27] (See Methods). The simulations were designed based on public information on the geothermal field operation (openei.org; maps.conservation.ca.gov/doggr) and previous studies[25,26,28]. The Coso geothermal field consists of over 100 wells, which were developed sequentially over the 30 years of production, in an area with multiple strike-slip (dominant in the main field area) and normal (dominant in the east flank area) faults (Fig. 1a inset). The first successful production well was completed in 1981, but large-scale production started in 1987 once the development of the main field was completed. The development of the east flank area started in the early 2000s[26,28]. We consider a simplified setting consistent with the size of the developed area and constrained by reported flow rates and energy production. Our model consists of 50 wells (25 injectors and 25 producers at depths of 1800m and 1300m) in a 4km × 4km × 3km reservoir, which is embedded within a 30km × 30km × 18km domain (Extended Data Fig 4). The reservoir and cap are assigned a bulk Mohr-Coulomb rheology, with the cohesion of 2 MPa and a friction coefficient of 0.6 (additionally 0.3), with the medium outside the reservoir and cap considered fully elastic. All elements are assigned a volumetric thermal contraction coefficient of 6.0×10^{-5}/K, consistent with laboratory measurements at 250°C[29]. Vertical stress is controlled by gravitational loading, and horizontal stresses are applied on the boundary consistent with a previous study of the local stress field[25,26,28]. (see Methods)

Reservoir cooling is mainly driven by fluid advection associated with the cold-water injection and depends, therefore, primarily on the flow rate. Hence, the flow rate is a dominating factor in defining reservoir temperature change. The data reported by the operator show production rates nearly twice as large as injection rates (Fig. 2a). The excess production must have been balanced by either a reduction of the pore volume or by an influx of groundwater in the reservoir. The cumulated excess volume of $\sim5.3\times10^{8}$ m^3 (assuming 1 ton ~ 1 m^3) would require an unrealistic pressure drop of the order of 400MPa (assuming a ~2km×2km×4km reservoir with a bulk modulus of 13GPa). The excess production was thus likely compensated by a significant groundwater supply. This inference is consistent with geochemical evidence for recharge from a shallow cold aquifer and from regional groundwater[30]. It also implies that the reservoir pore space is partly filled with steam due to vaporization. Because our simulation assumes a hydraulically closed domain boundary and single-phase flow, fitting both the production and injection data would require an unreasonably large pore pressure drop. We, therefore, carried out simulations targeted to fit either the production (Fig. 2a) or the injection rates. We choose the first scenario as a reference as it is probably more realistic because the excess production is likely coming from colder surrounding areas or groundwater. We consider the second scenario provides a lower bound on thermal effects (Extended Data Fig. 5). We note that even our reference scenario may underestimate thermal contraction because it ignores the cooling effect of evaporation implied by the continuous increase of the steam fraction in the produced flow over the operation period[31].

Our simulations account for the continuous pressure decline *via* controlling the injection and production pressure (Extended Data Fig. 6). The resulting pressure drop after 30 years is approximately ~5.5MPa within the reservoir and gradually decreases beyond it (Extended Data Fig. 6b). The predicted pressure drop rate (~0.18 MPa/year) matches the reported pressure decline rate (~0.17 MPa/year during 2012~2014) [17]. Our simulations show that even if heat extraction is driven only by the injection flow rate, the effect of the pore pressure drop on stress changes is only a fraction of the thermal stresses.

In our reference simulation, the production temperature drops from 250°C (year 0) to between 150 and 210°C after 30 years (Fig. 2b). This simulation initially yields electricity generation of ~170 MW which declines over time to ~50 MW, assuming an average geothermal power plant efficiency of 12%[32]. This estimate is somewhat smaller than the reported power output capacity (230MW)[13], but it gets close if we assume 16% efficiency, which is at the upper bound of the efficiency of double-flash power plants, which is the technology used at the Coso[32]. This comparison shows that the heat extraction predicted in this simulation may be similar to, or slightly smaller than, that in reality.

Our reference simulation predicts cumulative surface LOS (Line Of Sight) displacement with a pattern and an amplitude (~65cm over 30 years) generally consistent with the InSAR data[14,33,34] (Fig. 2d,e,f). The peak deformation rate is ~3.0cm/year in our simulation (Fig. 2f), a value comparable to the observed value of ~3.5cm/year[14]. In general, our reference model provides a reasonable estimate of the strain change within the reservoir. We conducted additional simulations without thermal stress (Extended Data Fig. 8) and found that the pressure depletion could, in principle, contribute about 57% of total subsidence. Since the pressure drop takes place over a wider area than thermal cooling, the predicted surface subsidence by isothermal simulation is less localized and poorer fit to the satellite observations (Extended Data Fig. 8). This conclusion conflicts with the claim of Reinisch et al.[35]. that the subsidence in the Coso area is mostly pressure-driven. We note that if the pressure effect was dominant, it would fail to explain the sustained seismicity during the geothermal field operation at the Coso. Thermal effects help reconcile surface deformation with seismicity.

Thermal contraction results in a decrease of the compressive normal stresses, shifting the Mohr circles progressively toward the Mohr-Coulomb failure envelope (Fig. 3c). As a result, some reservoir areas fail, resulting in a gradual decrease in the differential stress. Failure limits the decrease of the minimum principal stress so that the Mohr circle shrinks in diameter, leading to a very significant decrease of shear stress in the reservoir (Fig. 3). We also conducted simulations assuming a purely elastic reservoir. There is no shear stress reduction in that case, but unrealistically large tensile stress reaches 18 MPa at the center of the reservoir (Extended Data Fig. 10). Such large tensile stresses would not be possible in reality, given the limited strength of the rocks comprising the reservoir.

Our model predicts that the shear stress drops from an initial value of ~9MPa to ~ 2.9MPa after 30 years of operation (Fig. 3d). Because friction tends to be reduced at higher temperatures, we also tested the case of lower internal friction of 0.3 compared to 0.6 for the reference model. We found that the final shear stress becomes even smaller with lower friction (Extended Data Fig. 9). The shear stress drop explains the relative gap of large aftershocks (M > 2) detected by the regional-seismic network in the Coso area in 2019. According to our simulation, the differential stress (the difference between the maximum and the minimum principal stresses, which are both horizontal) decreases from about 30 MPa to less than 10MPa (Extended Data Fig. 3d-f). At the injector depth, the maximum horizontal stress decreases gradually toward the vertical stress and even gets eventually lower. That evolution should, in principle, favor normal faulting events. Above the reservoir, at a depth shallower than ~1km, the vertical stress becomes smaller than the minimum horizontal stress so that thrust events should eventually be favored. This evolution of the stress field is qualitatively consistent with the increasing diversity of focal mechanisms observed during the geothermal field operation (Extended Data Fig. 3).

The predicted stress evolution is also consistent with the seismicity evolution. According to our model, the Coulomb stress on faults parallel to the Ridgecrest rupture initially increased by as much as 6.7 MPa due to thermal contraction of the reservoir (Fig. 3a). This stress increased rapidly, by ~0.6-0.8 MPa/year during the first 3 years before slowly decreasing towards <0.1 MPa/year at the end of the simulation (Fig 1d). Thus, the observed seismicity rate approximately follows the simulated Coulomb stress rate, as would be expected from a standard Coulomb failure model with instantaneous coseismic stress drop[36]. In reality, the response of the seismicity should be damped because earthquake nucleation is a time-dependent process[37]. The effect of nucleation can probably be neglected at the multi-annual time scale[36].

We note that Zhang et al[38] reported a poor sensitivity to dynamic triggering within the Coso Geothermal Field, an observation, however, questioned by recent studies[11,39]. In any case, the mechanism suggested by Zhang et al.[38], which calls for unclogging of fluid pathways and subsequent pore pressure equalization, is unlikely to explain the paucity of aftershocks at the Coso in 2019. A homogenous pore pressure should not have inhibited static triggering of earthquakes by the coseismic Coulomb stress increase.

While thermal contraction of the reservoir induced significant seismicity[1,40], it eventually contributed to depleting the stress available to drive the aftershocks during the Ridgecrest sequence. This destressing results from anelastic but mostly aseismic deformation. The total released seismic moment calculated by summing the scalar moments of the events[10] in the main field area is 2.1×10^{15} N·m. Using the Kostrov approach[41], this seismicity could account for a shear strain of at most 1.3×10^{-5}, a value estimated considering a 2km × 2km × 2km volume of rock with a shear modulus of 10GPa and assuming that all events occurred on parallel fault planes. This strain is about two orders of magnitude smaller than the maximum anelastic shear strain predicted by our simulation, $\sim1.1\times10^{-3}$ (Extended Data Fig. 11), implying that the deformation of the Coso reservoir was mostly aseismic. This agrees with the theoretical considerations and observational evidence during fluid injection experiments and geothermal operations[42-45] that faults tend to creep aseismically at low normal effective stresses.

We conclude that seismic and aseismic anelastic deformation induced by the geothermal operations at the Coso probably significantly released the shear stress initially available to drive earthquakes. The thermal destressing of the Coso area reduced aftershock productivity. Such destressing could, in principle, form a barrier to the propagation of a large earthquake. However, the shallow brittle-ductile transition beneath the broader Coso volcanic area seems a more likely cause of the arrest of the rupture in 2019, given that it stopped ~10 km away from the Geothermal field. The observed reduction in aftershock productivity may present a general model of the early-time potential, whether project-terminating triggered seismicity in deep geothermal projects[46-48] can be avoided and whether long-term seismicity[49] may ultimately ameliorate to acceptably reduced levels.

References from main text

1. Zang, A. *et al*. Analysis of induced seismicity in geothermal reservoirs – An overview. *Geothermics* **52**, 6–21 (2014) https://doi.org/10.1016/j.geothermics.2014.06.005.
2. Kim, K.-H. *et al*. Assessing whether the 2017 Mw 5.4 Pohang earthquake in South Korea was an induced event. *Science (80-.)*. **360**, 1007–1009 (2018) 10.1126/science.aat6081.
3. Ross, Z. E. *et al*. Hierarchical interlocked orthogonal faulting in the 2019 Ridgecrest earthquake sequence. *Science (80-.)*. **366**, 346–351 (2019) 10.1126/science.aaz0109.
4. Hardebeck, J. L. A Stress-Similarity Triggering Model for Aftershocks of the M w 6 . 4 and 7 . 1 Ridgecrest Earthquakes. *Bull. Seismol. Soc. Am.* **110**, 1716–1727 (2020) 10.1785/0120200015.
5. Chen, K. *et al*. Cascading and pulse-like ruptures during the 2019 Ridgecrest earthquakes in the Eastern California Shear Zone. *Nat. Commun.* **11**, 22 (2020) 10.1038/s41467-019-13750-w.
6. Hill, D. P. *et al*. Seismicity Remotely Triggered by the Magnitude 7.3 Landers, California, Earthquake. *Science (80-.)*. **260**, 1617 LP-1623 (1993) 10.1126/science.260.5114.1617.
7. Grigoli, F. *et al*. The November 2017 Mw 5.5 Pohang earthquake: A possible case of induced seismicity in South Korea. *Science (80-.)*. **360**, 1003–1006 (2018) 10.1126/science.aat2010.
8. Deichmann, N. & Giardini, D. Earthquakes Induced by the Stimulation of an Enhanced Geothermal System below Basel (Switzerland). *Seismol. Res. Lett.* **80**, 784–798 (2009) 10.1785/gssrl.80.5.784.
9. Hauksson, E. & Unruh, J. Regional tectonics of the Coso geothermal area along the intracontinental plate boundary in central eastern California: Three-dimensional Vp and Vp/Vs models, spatial-temporal seismicity patterns, and seismogenic deformation. *J. Geophys. Res. Solid Earth* **112**, (2007) doi:10.1029/2006JB004721.
10. Hauksson, E., Yang, W. & Shearer, P. M. Waveform Relocated Earthquake Catalog for Southern California (1981 to June 2011). *Bull. Seismol. Soc. Am.* **102**, 2239–2244 (2012) 10.1785/0120120010.
11. Kaven, J. O. Seismicity Rate Change at the Coso Geothermal Field Following the July 2019 Ridgecrest Earthquakes. *Bull. Seismol. Soc. Am.* (2020) doi:10.1785/0120200017.
12. Blake, K. *et al*. Updated Shallow Temperature Survey and Resource Evolution for the Coso Geothermal Field. *Proc. World Geotherm. Congr. 2020, Reykjavik, Iceland, April 26- May 2* (2020).
13. Bertani, R. World geothermal power generation in the period 2001–2005. *Geothermics* **34**, 651–690 (2005) https://doi.org/10.1016/j.geothermics.2005.09.005.
14. Fialko, Y. & Simons, M. Deformation and seismicity in the Coso geothermal area, Inyo County, California: Observations and modeling using satellite radar interferometry. *J. Geophys. Res. Solid Earth* **105**, 21781–21793 (2000) doi:10.1029/2000JB900169.

15. Reinisch, E. C., Cardiff, M., Kreemer, C., Akerley, J. & Feigl, K. L. Time-Series Analysis of Volume Change at Brady Hot Springs, Nevada, USA, Using Geodetic Data From 2003–2018. *J. Geophys. Res. Solid Earth* **125**, e2019JB017816 (2020) doi:10.1029/2019JB017816.
16. Wicks, C. W., Thatcher, W., Monastero, F. C. & Hasting, M. A. Steady state deformation of the Coso Range, east central California, inferred from satellite radar interferometry. *J. Geophys. Res. Solid Earth* **106**, 13769–13780 (2001) doi:10.1029/2001JB000298.
17. Blankenship, D. A. *et al*. Frontier Observatory for Research in Geothermal Energy: Phase 1 Topical Report West Flank of Coso, CA. doi:10.2172/1455367 10.2172/1455367.
18. Goebel, T. H. W. & Brodsky, E. E. The spatial footprint of injection wells in a global compilation of induced earthquake sequences. *Science (80-.).* **361**, 899–904 (2018) 10.1126/science.aat5449.
19. Goebel, T. H. W., Weingarten, M., Chen, X., Haffener, J. & Brodsky, E. E. The 2016 Mw5.1 Fairview, Oklahoma earthquakes: Evidence for long-range poroelastic triggering at >40 km from fluid disposal wells. *Earth Planet. Sci. Lett.* **472**, 50–61 (2017) https://doi.org/10.1016/j.epsl.2017.05.011.
20. Sanyal., S., Menzies, A., Granados, E., Sugine, S. & Gentner, R. Long term testing of geothermal wells in the coso hot springs KGRA. *Proceedings, twelfth Work. Geotherm. Reserv. Eng. Stanford Univ. Stanford, California, January 20-22* (1987).
21. Im, K., Elsworth, D., Guglielmi, Y. & Mattioli, G. S. Geodetic imaging of thermal deformation in geothermal reservoirs - production, depletion and fault reactivation. *J. Volcanol. Geotherm. Res.* **338**, (2017) 10.1016/j.jvolgeores.2017.03.021.
22. Rutqvist, J., Wu, Y.-S., Tsang, C.-F. & Bodvarsson, G. A modeling approach for analysis of coupled multiphase fluid flow, heat transfer, and deformation in fractured porous rock. *Int. J. Rock Mech. Min. Sci.* **39**, 429–442 (2002) https://doi.org/10.1016/S1365-1609(02)00022-9.
23. Segall, P. & Fitzgerald, S. D. A note on induced stress changes in hydrocarbon and geothermal reservoirs. *Tectonophysics* **289**, 117–128 (1998) https://doi.org/10.1016/S0040-1951(97)00311-9.
24. Yang, W., Hauksson, E. & Shearer, P. M. Computing a Large Refined Catalog of Focal Mechanisms for Southern California (1981–2010): Temporal Stability of the Style of Faulting. Bull. Seismol. Soc. Am. 102, 1179–1194 (2012) 10.1785/0120110311.
25. Feng, Q. & Lees, J. M. Microseismicity, stress, and fracture in the Coso geothermal field, California. *Tectonophysics* **289**, 221–238 (1998) https://doi.org/10.1016/S0040-1951(97)00317-X.
26. Davatzes, N. C. & Hickman, S. H. Stress and Faulting in the Coso Geothermal Field : Update and Recent Results from the East Flank and Coso Wash. *Proceedings, thirty-first Work. Geotherm. Reserv. Eng.* (2006).
27. Taron, J., Elsworth, D. & Min, K.-B. Numerical simulation of thermal-hydrologic-mechanical-chemical processes in deformable, fractured porous media. *Int. J. Rock Mech. Min. Sci.* **46**, 842–854 (2009) https://doi.org/10.1016/j.ijrmms.2009.01.008.
28. Rose, P. *et al*. An Enhanced Geothermal System at Coso , California — Recent Accomplishments. *Proc. World Geotherm. Congr. 2005 Antalya, Turkey* (2005).
29. Cooper, H. W. & Simmons, G. The effect of cracks on the thermal expansion of rocks. *Earth Planet. Sci. Lett.* **36**, 404–412 (1977) https://doi.org/10.1016/0012-821X(77)90065-6.
30. Spane Jr, F. . Hydrogeologic Investigation of Coso Hot Springs, Inyo County, California. *Tech. Report; Hydro-Search Inc. Reno, NV, USA* (1978).

31. MHA Environmental Consulting. Coso operating company hay ranch water extraction and delivery system Conditional use permit (CUP 2007-003) application (2008).
32. Zarrouk, S. J. & Moon, H. Efficiency of geothermal power plants: A worldwide review. *Geothermics* **51**, 142–153 (2014) https://doi.org/10.1016/j.geothermics.2013.11.001.
33. Ali, S. T. *et al*. Geodetic measurements and numerical models of deformation: Examples from geothermal fields in the western united states. *PROCEEDINGS, 41st Work. Geotherm. Reserv. Eng. Stanford Univ. Stanford, California, Febr. 22-24* (2016).
34. Wang, K. & Bürgmann, R. Co< and Early Postseismic Deformation Due to the 2019 Ridgecrest Earthquake Sequence Constrained by Sentinel< 1 and COSMO< SkyMed SAR Data. *Seismol. Res. Lett.* (2020) doi:10.1785/0220190299
35. Reinisch, E. C., Ali, S. T., Cardiff, M., Kaven, J. O. & Feigl, K. L. Geodetic Measurements and Numerical Models of Deformation at Coso Geothermal Field , California , 2004–2016. *Remote Sens.* (2020) doi:10.3390/rs12020225 10.3390/rs12020225.
36. Ader, T. J., Lapusta, N., Avouac, J.-P. & Ampuero, J.-P. Response of rate-and-state seismogenic faults to harmonic shear-stress perturbations. *Geophys. J. Int.* **198**, 385–413 (2014) 10.1093/gji/ggu144.
37. Dieterich, J. A constitutive law for rate of earthquake production and its application to earthquake clustering. *J. Geophys. Res. Solid Earth* **99**, 2601–2618 (1994) doi:10.1029/93JB02581.
38. Zhang, Q. *et al*. Absence of remote earthquake triggering within the Coso and Salton Sea geothermal production fields. *Geophys. Res. Lett.* **44**, 726–733 (2017) doi:10.1002/2016GL071964.
39. Alfaro-Diaz, R., Velasco, A. A., Pankow, K. L. & Kilb, D. Optimally Oriented Remote Triggering in the Coso Geothermal Region. *J. Geophys. Res. Solid Earth* **125**, e2019JB019131 (2020) https://doi.org/10.1029/2019JB019131.
40. Hauksson, E. & Jones, L. M. Seismicity, Stress State, and Style of Faulting of the Ridgecrest< Coso Region from the 1930s to 2019: Seismotectonics of an Evolving Plate Boundary Segment. *Bull. Seismol. Soc. Am.* **110**, 1457–1473 (2020) 10.1785/0120200051.
41. Kostrov, V. Seismic moment and energy of earthquakes, and seismic flow of rock. *Izv. Acad. Sci. USSR Phys. Solid Earth* 23–44 (1974).
42. Cornet, F. H., Helm, J., Poitrenaud, H. & Etchecopar, A. Seismic and Aseismic Slips Induced by Large-scale Fluid Injections. *pure Appl. Geophys.* **150**, 563–583 (1997) 10.1007/s000240050093.
43. Guglielmi, Y., Cappa, F., Avouac, J.-P., Henry, P. & Elsworth, D. Seismicity triggered by fluid injection-induced aseismic slip. *Science (80-.).* **348**, 1224–1226 (2015) 10.1126/science.aab0476.
44. Wei, S. *et al*. The 2012 Brawley swarm triggered by injection-induced aseismic slip. *Earth Planet. Sci. Lett.* **422**, 115–125 (2015) 10.1016/j.epsl.2015.03.054.
45. Cappa, F., Scuderi, M. M., Collettini, C., Guglielmi, Y. & Avouac, J.-P. Stabilization of fault slip by fluid injection in the laboratory and in situ. *Sci. Adv.* **5**, (2019) 10.1126/sciadv.aau4065.
46. Kwiatek, G. *et al*. Controlling fluid-induced seismicity during a 6.1-km-deep geothermal stimulation in Finland. *Sci. Adv.* **5**, (2019) 10.1126/sciadv.aav7224.

47. Hillers, G. *et al*. Noise-based monitoring and imaging of aseismic transient deformation induced by the 2006 Basel reservoir stimulation. *Geophysics* **80**, KS51-KS68 (2015) 10.1190/geo2014-0455.1.
48. Häring, M. O., Schanz, U., Ladner, F. & Dyer, B. C. Characterisation of the Basel 1 enhanced geothermal system. *Geothermics* **37**, 469–495 (2008) https://doi.org/10.1016/j.geothermics.2008.06.002.
49. Gan, Q. & Elsworth, D. Thermal drawdown and late-stage seismic-slip fault reactivation in enhanced geothermal reservoirs. *J. Geophys. Res. Solid Earth* **119**, 8936–8949 (2014) https://doi.org/10.1002/2014JB011323.

Main Figure legends

Fig. 1. Ridgecrest aftershock and prior seismicity in the Coso area. a: Relocated seismicity[10] (M_w>1) before (gray circles, from 2010 on) and after (blue circles, until the end of 2019) the 2019 M_w 7.1 mainshock (see the yellow star for the location of the epicenter). The black line denotes the surface ruptures of the M_w 7.1 and 6.4 earthquakes of 2019[3]. **Inset**: zoomed-in view of the Coso geothermal field. Solid lines represent strike-slip faults parallel to surface ruptures of Ridgecrest earthquakes (red) and normal (blue) faults[25,26,] and triangles denote geothermal well locations (maps.conservation.ca.gov/doggr). The red symbol in the inset represents principal stress orientations and their relative magnitude (lines: horizontal, circle: vertical)[25,26]. **b:** Static Coulomb stress change due to the M_w 7.1 2019 earthquakes calculated for right-lateral fault parallel to main faults ruptured in these events (red fault in Fig.1 inset). We used source models derived from remote sensing and high rate GPS data[5] assuming a coefficient of friction 0.6. Dots denote Ridgecrest aftershocks. **c:** Depth distribution of earthquakes of section XX' in panel a (all events in the orange box of Fig 1a) with coseismic slip distribution[5] (red). **d:** Yearly rate of M>1 earthquakes (i.e., gray circles in a&c) of main field (black line; Extended Data Fig. 1c+d+e) and entire the Coso area (main field + east flank, gray line) and with Coulomb stress change rate at the center of the reservoir simulated in this work (red; Fig. 3a). (see Extended Data Fig. 1,2,&3 for detailed seismicity history).

Fig. 2. **Production, power generation, and surface subsidence for our reference simulation. a:** Reported injection and production flow rates from the Coso field (thin lines) with superimposed simulation results (bold lines). The onset of production is set to 1/1/1989 in the simulation. **b:** Predicted temperature change since the onset of production at all 25 producing wells. **c:** Time evolution of earthquakes (M>1) depth within the Coso field. The migration toward greater depth is consistent with the cooling of the reservoir. **d**: Cumulative LOS displacement over the Coso area recovered from InSAR measurements between May 1996 and June 1998[14]. **e:** Predicted cumulative LOS displacement after 30 years of production. The arrow shows the LOS unit vector (0.38, -0.09, and 0.92)[14] surface deformation (see Extended Data Fig. 7 for separate x, y, z components). **f:** Time evolution of maximum LOS displacement (black line) and observed LOS displacement rates (blue solid lines)[14,33,34] with their extrapolations (blue dashed lines).

Fig. 3. **Simulation of stress changes due to thermal contraction, pore pressure changes, and anelastic failure of the reservoir. a:** Coulomb stress change at the end of the simulation (year 30) calculated on faults parallel to the M_w 7.1 rupture on a cross-section through the reservoir area (see inset). **b**: Shear stress at the end of the simulation (year 30) for the same cross-section. **c**: Mohr circle representation of the evolution of stress at the center of the reservoir during the simulation (stresses averaged along the yellow line in **a**&**b**). The Mohr circles don't touch the failure envelope because failure occurs only in a fraction of the reservoir volume, close to the injection wellbore. The Gray dashed line denotes the input failure criteria in this simulation. **d**: Time series of shear stress change at the center of the reservoir (averaged along yellow line in **a**&**b**).

Methods

We used Tough-FLAC [27] to simulate thermo-hydro-mechanical processes during the geothermal operation. Stress changes within the reservoir depending on the mechanical response of the surrounding medium[21,50]. We, therefore, consider a simulation domain (30km × 30km × 18km) substantially larger than the geothermal reservoir (4km × 4km × 3km) itself. The reservoir size is similar to the currently developed area of the Coso geothermal field.

Extended Data Fig. 4 shows the geometry and initial stress field. The domain is meshed into 13312 blocks, which are divided into either reservoir or host blocks. All blocks are assigned a volumetric thermal contraction coefficient 6.0×10^{-5} /K, the bulk modulus of 13GPa, and Poisson's ratio of 0.2. The magnitude of thermal expansion is consistent with the experimental result with quartz-rich rock at a temperature of 250 °C[29]. Reservoir blocks (blue) are embedded at a depth between 1km ~ 4km. Reservoir (blue) and upper host (dark green) are assumed to fail according to the Mohr-Coulomb criteria with a friction coefficient of 0.6 and cohesion of 2MPa. Lower host rock blocks (light green) are fully elastic. To achieve stable flowrate and electricity generation, we assumed constant permeability over the entire domain. Reservoir elements have high permeabilities of 16md and 10md for higher and lower flow rate cases, respectively (Extended Data Fig. 5). The host (both lower and upper) block has a much smaller permeability of 0.05md. The permeabilities were tuned to yield a production rate comparable to the Coso field (openei.org). See Extended Data Table 1 for model parameters.

The stress field accounts for gravity and tectonic loading. Gravitational body forces are calculated assuming an effective density (rock density – water density) of 1400kg/m^3. The stress field is assumed initially homogeneous with maximum and minimum horizontal stresses of 150% and 50% of the vertical stress, respectively, based on a previous study of the local stress field[25,26]. The maximum principal stress strikes initially N20°E, which is oriented at 65° from the right-lateral strike-slip faults (Extended Data Fig. 4 inset). Rollers with shear stress are applied at the domain boundary except at the ground surface, which is assumed traction-free. We tested both roller and constant stress boundary conditions at the domain boundary and found no significant differences, confirming that the model domain is large enough. To reduce the computational cost, we assumed an initial uniform temperature of 250°C over the domain. Also, since water density and viscosity are not strongly dependent on pressure, the pressure here represents the overpressure from the hydraulic pressure (gravitational flow is ignored).

Accordingly, the stresses in this simulation represent effective stresses (stress minus fluid pressure).

The Coso geothermal field consists of over 100 wells developed sequentially over the 30 years of production in an area with multiple strike-slip faults. We simplified the field into 50 wellbores. The wells include 25 injectors and 25 producers, forming a 5-spot pattern accessing two depths layers (1300m and 1800m; Extended Data Fig. 4). The distance between the injectors and producers is ~500m but slightly more closely spaced at the center of the reservoir (see Extended Data Fig. 4 well location). A Peaceman well-block pressure model[51] is employed with a virtual wellbore radius of 10cm and a Skin factor -4 located within the well block as in Extended Data Fig.4. The initial wellbore pressure is set to 5 MPa overpressure and -1 MPa underpressure at the injector and producer wells, respectively (Extended Data Fig. 6a), and declines with time at a different rate to achieve target flow rate (Fig 2a) and pressure drop (Extended Data Fig. 6).

We acknowledge that our simulation is an oversimplification of reality. The more realistic simulation should consider the distribution of initial pressure and temperature. In reality, the geothermal gradient is much smaller, even right in the vicinity of the Coso area[17]. This temperature distribution affects reservoir temperature evolution by the fluid influx from the surrounding area. The influx from the deeper hot zone will increase the reservoir temperature, but the influx from all other surroundings will cool down the reservoir. The cooling effect is likely much larger than the heating effect because the cooler zone has larger contact to the reservoir, and also cold water is continuously supplied from precipitations and aquifer flow. Although smaller than the reality, our simulation also has a considerable fluid influx (overproduction) from the surrounding area (fig. 2a). The temperature of the influx in our simulation is likely higher than the reality since we assume a uniform high temperature (250°C) even at this surrounding cooler area. Accordingly, if we use a more realistic initial temperature distribution, a larger thermal destressing is expected due to the cold-water influx from the surroundings. Furthermore, the application of a realistic pressure gradient would induce the endothermic effect of evaporation in and above the reservoir and therefore also increase the cooling effect. Overall, we expect the application of realistic pressure and temperature gradient will enhance the thermal destressing effect over that in our simulation result.

The nearly uniform thermal depletion in our simulation is not expected in a highly fractured real reservoir. Also, a significant change in the permeability would be expected[21] with production. In reality, the thermal depletion is dominant in the vicinity of existing fractures due to the high permeability and thermal stimulation[21]. Therefore, the fracture thermal depletion can become wider than predicted in our idealized depletion model. Given that the subsidence predicted by our model is comparable in extent and rate with the available observations of surface deformation, we believe that, even with these simplifications, our model provides a reasonable first-order estimate of the stress changes imparted by geothermal operations at the Coso.

References in Methods

50. Eshelby, J. D. The determination of the elastic field of an ellipsoidal inclusion, and related problems. Proc. R. Soc. London. Ser. A. Math. Phys. Sci. 241, 376–396 (1957) 10.1098/rspa.1957.0133.

51. Peaceman, D. W. Interpretation of Well-Block Pressures in Numerical Reservoir Simulation With Nonsquare Grid Blocks and Anisotropic Permeability. *Soc. Pet. Eng. J.* **23**, 531–543 (1983) 10.2118/10528-PA.
52. Cappa, F. & Rutqvist, J. Modeling of coupled deformation and permeability evolution during fault reactivation induced by deep underground injection of CO2. *Int. J. Greenh. Gas Control* **5**, 336–346 (2011) https://doi.org/10.1016/j.ijggc.2010.08.005.
53. Frohlich, C. Triangle diagrams: ternary graphs to display similarity and diversity of earthquake focal mechanisms. *Phys. Earth Planet. Inter.* **75**, 193–198 (1992) https://doi.org/10.1016/0031-9201(92)90130-N.

Acknowledgments:

We are grateful to Roland Burgmann, Ole Kaven and one anonymous reviewer for their insightful comments and suggestions which helped improved this manuscript substantially. This study was supported by the National Science Foundation via the IUCR center Geomechanics and Mitigation of Geohazards (award #1822214) and via the Southern California Earthquake Center.

Author contributions:

K.I. carried out the data analysis and numerical simulations. E.R.H. provided the coseismic Coulomb stress changes. D.E. provided the simulator THOUGH-FLAC. K.I. and J.-P.A. designed the study and wrote the article. All authors edited the manuscript.'

Data availability

Seismic catalog[10] is publicly available at Southern California Earthquake Data Center (https://scedc.caltech.edu/data/alt-2011-dd-hauksson-yang-shearer.html). Coso field well location and flow rate data is available at California Department of Conservation homepage (https://maps.conservation.ca.gov/doggr/wellfinder & https://www.conservation.ca.gov/calgem/geothermal/manual/Pages/production.aspx). Simulation result data are available in and in Caltech data repository (https://doi.org/10.22002/D1.1455). Source data are available in this paper.

Code availability

TOUGH-FLAC coupled simulator and all input files available at the Caltech data repository (https://doi.org/10.22002/D1.1455)

Competing interests

The authors declare no competing interests.

Extended Data Legends

Extended Data Table 1.

Title: **Simulation model parameters**

Footnote: *1.6×10^{-14} m^2 and 1.0×10^{-14} m^2 for high and low flow rate cases, respectively.

Extended Data Fig. 1

Seismicity before and after the Ridgecrest mainshock of July 5th 2019 within and around the Coso area. We divided the area into different domains. (**a-d**): relocated seismicity[10] of all magnitude before (gray circles, 2010 – M_w 7.1 mainshock) and after (blue circles, M_w 7.1 mainshock – end of 2019) the Ridgecrest earthquake. We compare the spatial distribution (**a-d**) and cumulative magnitude-frequency distribution (**e-h**) of earthquakes before (black) and after (blue) the mainshock for the Coso volcanic area (**a**, **e**), Cactus Flat (**b**, **f**), Coso geothermal field (**c**, **g**), and the NW edge of the M_w 7.1 event (**d**, **h**). Red rectangles in the panel a outline the locations of each plot. Black triangles in panel c denote geothermal well locations. The density of aftershocks above the detection threshold (M>1) is about 2 orders of magnitude lower within the Coso Geothermal Field (**c**) than in the immediately surrounding areas (**b**, **d**). A similar result is reported in a previous study[4].

Extended Data Fig. 2

Seismicity history in the Coso area. a: Distribution of seismicity of all events magnitude M >1[10]. **b:** Seismicity history over the entire Coso area. **c-f:** Seismicity history of each fault zone corresponding to the area denoted in **a**. The fault zones are selected based on the expression of the seismic cloud. The Coso main field consists of **c**, **d**, and **e**. The east flank area is **f**.

Extended Data Fig. 3

Change of focal mechanism in the Coso main field area and effective stress changes predicted by the simulation. Rake angle (**a**) shows the proportion of normal faulting (-120° ~ -60°) increases with time. Ternary plots[53] (**b**, **c**) show that the formal mechanism is more diverse with increased normal faulting in the later operation period (**c**, 2001-2019) than earlier period (**b**, 1981-2000). (**d-f**): Time-dependent maximum horizontal (red), minimum horizontal (blue), and vertical (black) stress at different depths calculated as an average along a 1 km baseline at the center of the reservoir at each depth. The stresses within the reservoir (**e**,**f**) decline with time. But the rate of the vertical stress decline is lower than the decline of the maximum horizontal stresses. The simulation result predicts an increase in the proportion of normal faulting and diversity of focal mechanism as observed in **a-c**.

Extended Data Fig. 4

Model description. Blue, dark green, and light green blocks represent the reservoir, upper host, and lower host elements, respectively. The right-hand side shows the repeating 5-spot pattern of injectors (triangles) and producers (circles). **Inset**: Initial horizontal stresses calculated from Coso field data (Fig. 1a inset). Vertical stress is calculated as gravitational stress for an effective density of 1400 kg/m^3 at every time step. The x-axis is chosen parallel to the dominant fault orientation in the Main field (Fig. 1a inset), which is parallel to the main fault ruptured in the M_w 7.1 Ridgecrest earthquake. Roller and shear stress boundaries are applied corresponding to the initial stress, as shown in the inset. The ground surface is stress-free.

Extended Data Fig. 5

Simulation results with lower flow rate. Simulation result identical to Fig. 2 but with a lower flow rate set to match the injection rate *via* permeability reduction. Other parameters are identical to our reference simulation (Fig. 2). **a:** Reported injection and production flow rates from the Coso field (thin lines) and simulation results (bold lines). **b**: Ground deformation recovered from InSAR measurements between May 1996 and June 1998[14]. **c:** Cumulative LOS surface displacement at the end of the simulation (year 30). **d:** Time evolution of maximum LOS displacement (black line) and observations (blue solid lines)[14,33,34] with their extrapolations (blue dashed lines). **e**: Shear stress at the end of the simulation (year 30) in the orientation parallel to the M_w 7.1 rupture in the reservoir area (see inset).

Extended Data Fig. 6

Wellbore and reservoir pressure. **a**: Pressure change at wellbores (black straight line) and well blocks (the block where the imaginary wellbore is embedded; colored lines). The pressure gap between the wellbore and well block is larger at injection than production due to the low temperature and subsequent low fluid viscosity. **b**: Pressure drop distribution at the end of the simulation. The white rectangle denotes the 4km × 4km × 3km reservoir area. The pressure drops by ~5.5MPa within the reservoir, and the halo of pressure drop extends beyond the reservoir area.

Extended Data Fig. 7

Predicted surface displacements at the end of the reference simulation. Displacement along the x- (**a**), y- (**b**), and z-axes (**c**), and LOS displacement (**d**). Panel **d** is identical to Fig. 2e. Arrow denotes the azimuth of the LOS vector, the unit vector towards the satellite, (0.38, -0.09, 0.92)[14].

Extended Data Fig. 8

Predicted surface deformation due to pore pressure change alone. **a**: LOS surface displacement recovered from InSAR measurements between May 1996 and June 1998. (modified from ref. *9*). **b**: Predicted LOS surface displacement at the end of the isothermal simulation. All parameters are identical to the reference simulation, which accounts for thermal strain (i.e., Fig. 2). **c:** Time evolution of maximum LOS displacement of the isothermal (red) and non-isothermal (black, Fig. 2f) simulations together with observations (blue solid lines)[14,33,34] and their interpolations (blue dashed lines). Subsidence absent thermal stresses represent the pressure depletion effect alone. **d**: Observed and predicted ground displacements projected along the Line Of Sight (LOS, arrow in inset of panel b) of the of satellite SAR images[14,33]. Each profile was normalized. The black solid line and inset are from our reference simulation (Fig. 2), and the red solid line is from isothermal (no thermal strain) simulation. The curves are normalized relative to maximum displacement ~65cm and ~35cm for the reference and no-thermal stress cases, respectively (panel c). The Fialko and Simons[14] case is measured between September 1993 to May 1996 with a maximum displacement of ~8cm (WE) and ~5cm (SN), and the Ali et al.[33] case is measured between February 2008 to October 2009 with a maximum displacement of ~2cm.

Extended Data Fig. 9

Predicted stress changes in a simulation with reduced friction. The simulation geometry and parameters are identical to the reference simulation (Fig. 3) except for a lower internal friction coefficient of 0.3. **a:** Coulomb stress change at the end of the simulation (year 30) calculated for faults parallel to the main rupture (see inset). **b**: Shear stress at the end of the simulation (year 30). Shear stress in the reservoir area (white rectangle in panel b) is strongly depleted due to rock failure. **c**: Mohr circle representation of stress changes during the simulation. Maximum and minimum effective normal stress is calculated at the center of the reservoir (stresses averaged along the yellow line in a&b). The Mohr circle at year 0 is smaller than for the higher friction cases (Fig. 3c) due to initial failure. The Gray dashed line denotes the input failure criterion in this simulation. **d**: Time series of shear stress change at the center of the reservoir (averaged along yellow line in a&b).

Extended Data Fig. 10

Comparison between fully elastic and Mohr-Coulomb failure model. **a** is an identical plot to Fig. 3**c**. **b** is an identical plot to **a,** except that the reservoir is fully elastic (no failure) in this case. It shows that when the reservoir is fully elastic, normal stresses become impossibly large in tension if failure and the resulting stress drop is neglected. **c** and **d** show normal and shear stress evolution relative to the Ridgecrest fault orientation (see Extended Data Fig. 4 inset for orientation) at1500m depth for the Mohr-Coulomb failure model the fully elastic model, respectively. With the failure model, the stresses naturally approach zero over time (**c**), as a result of shear and tensile failure, but in the fully elastic case, normal stresses transit through zero and become highly tensile when the shear stress drops, as a result of failure being ignored. The wiggles within the well pattern area of the reservoir are due to the non-uniform distribution of temperature driving differential thermal stresses.

Extended Data Fig. 11

Cumulative shear strain at the conclusion of the reference simulation (after 30 years of production). The largest strain change occurs within the well pattern area, where the temperature change is most significant. The maximum shear strain is ~ 1.1×10^{-3}, which is approximately two orders of magnitude larger than the strain released by seismicity as estimated from the sum of all seismic moments (see text).

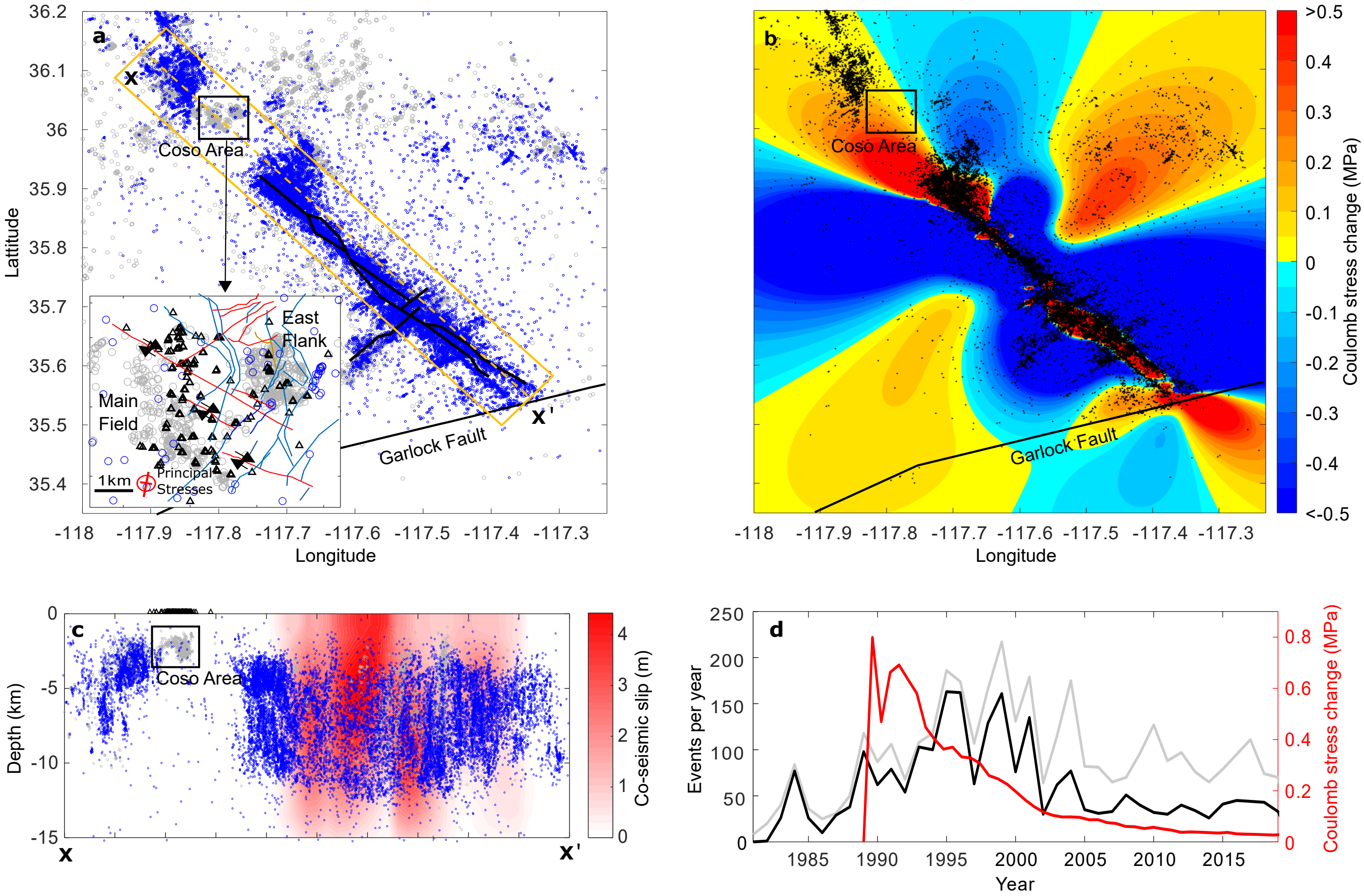

a
X
X'
Coso Area
East Flank
Main Field
1km
Principal Stresses
Garlock Fault
Latitude
Longitude
b
Coso Area
Garlock Fault
Longitude
Coulomb stress change (MPa)
c
Coso Area
Depth (km)
Co-seismic slip (m)
X
X'
d
Events per year
Coulomb stress change (MPa)
Year

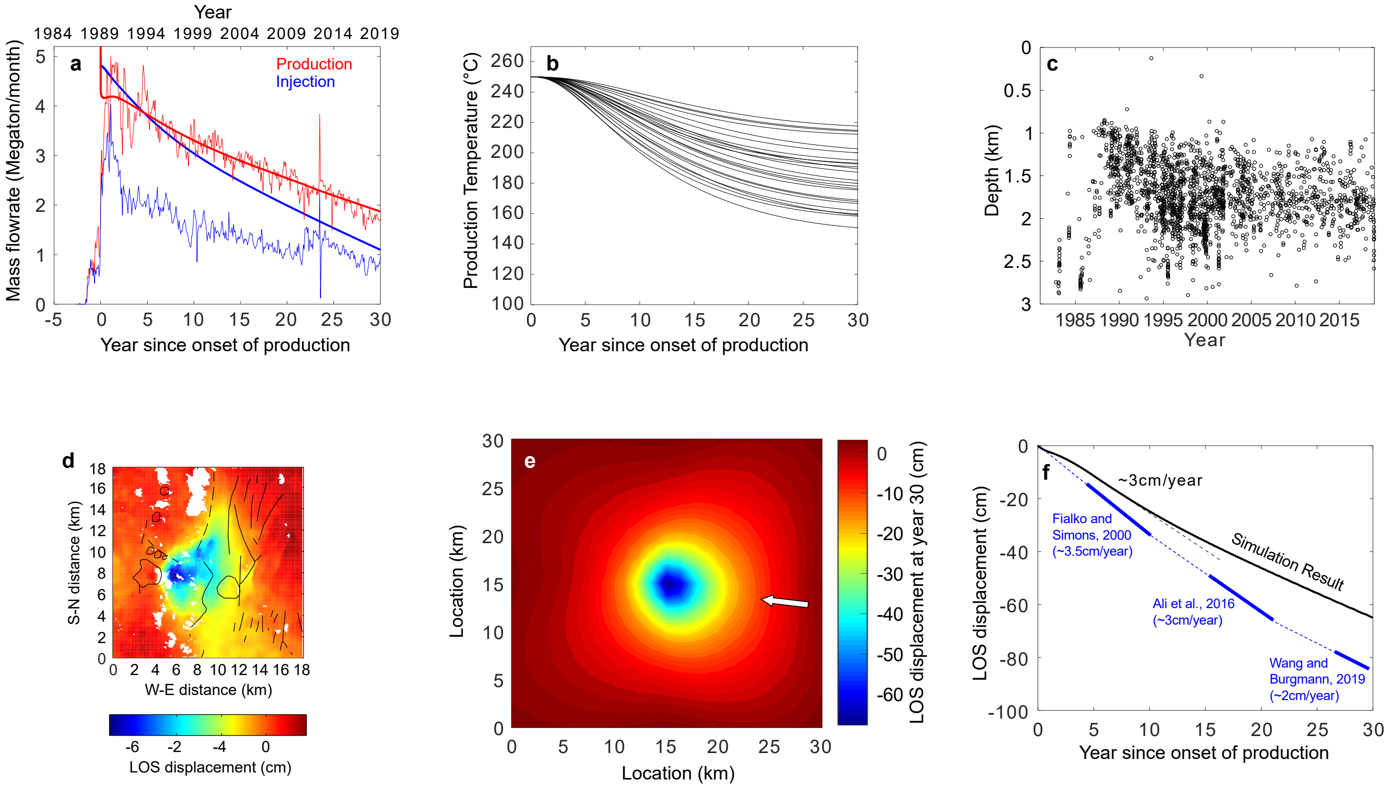

a
Year
1984 1989 1994 1999 2004 2009 2014 2019
Mass flowrate (Megaton/month)
Production
Injection
Year since onset of production
b
Production Temperature (°C)
Year since onset of production
c
Depth (km)
Year
d
S-N distance (km)
W-E distance (km)
LOS displacement (cm)
e
Location (km)
LOS displacement at year 30 (cm)
f
~3cm/year
Fialko and Simons, 2000 (~3.5cm/year)
Simulation Result
Ali et al., 2016 (~3cm/year)
Wang and Burgmann, 2019 (~2cm/year)
LOS displacement (cm)
Year since onset of production

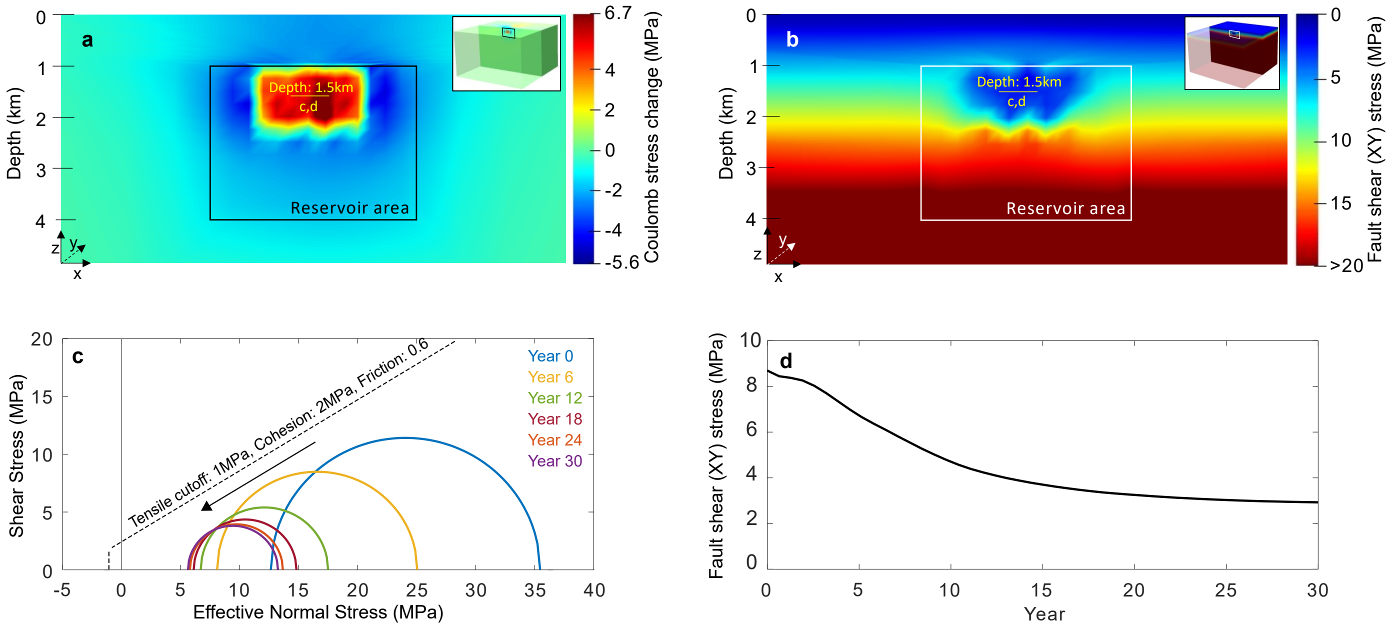

a
Depth (km)
Depth: 1.5km
c,d
Reservoir area
Coulomb stress change (MPa)
6.7
-5.6
b
Fault shear (XY) stress (MPa)
>20
c
Shear Stress (MPa)
Effective Normal Stress (MPa)
Tensile cutoff: 1MPa, Cohesion: 2MPa, Friction: 0.6
Year 0
Year 6
Year 12
Year 18
Year 24
Year 30
d
Fault shear (XY) stress (MPa)
Year